Synthesis and characterization of cyclometalated iridium(III) complexes containing benzoxazole derivatives and different ancillary ligands

Tsun-Ren Chen *

Department of Applied Chemistry and Life Science, National Pingtung University of Education, Pingtung 90003, Taiwan, ROC

ABSTRACT

The synthesis, structures, electrochemistry, and photophysics of a series of cyclometalated iridium(III) complexes based on benzoxazole derivatives and different β-diketonate ligands are reported. These complexes have a general formula $C^{\wedge}N_2Ir(LL')$ [where $C^{\wedge}N$ is a monoanionic cyclometalating ligand; 2-phenylbenzoxazolato (pbo), 2-(4-chlorophenyl)benzoxazolato (cpbo), 2-phenyl-5-chlorobenzoxazolato (pcbo), 2-(3,5-difluorophenyl)benzoxazole (fpbo), or 2-(2-naphthyl)benzoxazolato (nbo), and LL′ is an ancillary ligand; acetylacetonate (acac), dibenzoylmethanate (dbm), or 1,1,1,5,5,5-hexafluoroacetylacetonate (hfacac)]. The complexes $(pcbo)_2Ir(acac)$ (**3**), $(dfpbo)_2Ir(acac)$ (**4**), $(cpbo)_2Ir(dbm)$ (**7**), $(dfpbo)_2Ir(dbm)$ (**8**), and $(dfpbo)_2Ir(hfacac)$ (**9**) have been structurally characterized by X-ray crystallography. All of the complexes show reversible oxidation between 0.45 and 1.07 V, versus Fc/Fc+, and have short luminescence lifetime ($\tau = 0.1–1.3$ μs) at room temperature. Except complex **9**, the radiative decay rate (k_r) and nonradiative decay rate (k_{nr}) of the $(C^{\wedge}N)_2Ir(LL')$ complexes have been determined by using the lifetime and quantum efficiency. The k_r ranges between 2.0×10^3 and $3.0 \times 10^5 \text{ s}^{-1}$ and k_{nr} spans a narrower range of values (5.0×10^5 to $7.0 \times 10^6 \text{ s}^{-1}$).

© 2008 Elsevier B.V. All rights reserved.

1. Introduction

Recently, iridium complexes have been studied extensively because of their potential applications. For example, these complexes can be used as emissive dopants in organic light emitting devices (OLEDs) [1,2], catalysts for chemical reactions [3,4], photocatalysts for CO_2 reduction, photooxidants, and biological reagents [5]. Several research groups have reported that the heavy metal, iridium, in the complex can induce the intersystem crossing (ISC) by strong spin–orbit coupling, which leads to the mixing of the singlet and triplet excited states, and results in high phosphorescence efficiencies [6,7].

Benzoxazole and their derivatives have been comprehensively studied in recent years because of their high quantum yields [8], high non-linear optical effectiveness, biological activities [9,10], photo-stable properties [11], and capabilities to ligate transition metals [12]; hence, the benzoxazole compounds and their metallic complexes have been widely applied for use in chemistry and medicine [13]. In addition, the substituent in position 2 of the benzoxazole ring may be quite easily changed to modify the photophysical properties of the compound. For example, an electron-donor substituent on the phenyl ring of 2-phenylbenzoxazole can shift the absorption and emission spectra to the longer wavelengths, and an electron-withdrawing group can shift the photophysical spectra to the shorter wavelengths [9]. Therefore, to

investigate the effect of benzoxazole derivatives on the electrochemical and photophysical properties of iridium complexes, several kinds of benzoxazole derivatives were synthesized in this paper and used as cyclometalating ligands (abbreviated as $C^{\wedge}N$) to prepare a series of cyclometalated iridium(III) complexes, **1**–**9** (see Chart 1). Because benzoxazole derivatives possess high extinction coefficients and exhibit high fluorescence quantum yields [14,15], metal complexes containing benzoxazole derivatives as chelating ligands are expected to exhibit special properties and high quantum efficiencies. The complexes reported here have a general formula $(C^{\wedge}N)_2Ir(LL')$, in which the LL′ represents an ancillary ligand, and three kinds of β-diketonate ligands (acetylacetonate (acac), dibenzoylmethanate (dbm), and 1,1,1,5,5,5-hexafluoroacetylacetonate (hfacac), respectively) are used as the ancillary ligands to investigate the effect on the character of the corresponding iridium complexes. The photophysical properties of the complexes reported here in acetonitrile and dichloromethane were also studied in order to find out the relationships between structural properties and the spectroscopic properties, which can enable us to design more rational probes possessing required properties [9].

2. Results and discussion

2.1. Synthesis of materials

Scheme 1 shows the synthesis of the ligands and the iridium complexes. By Philips′ condensation, a series of benzoxazole

* Tel.: +886 8 7226141 800.
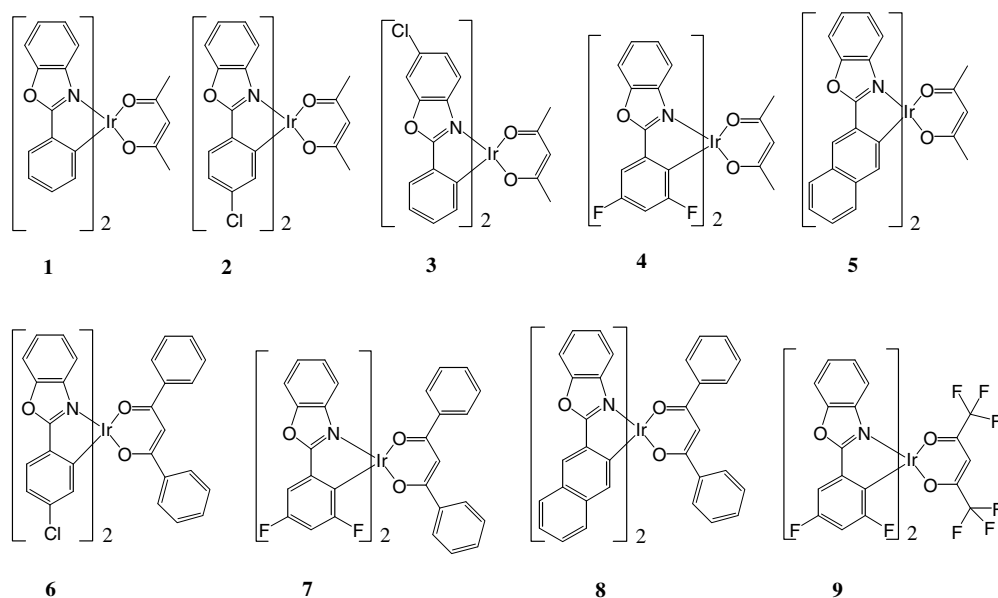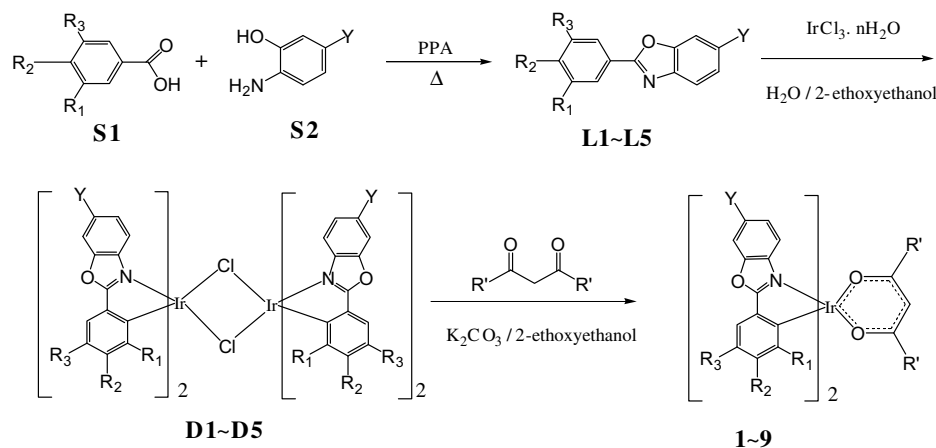E-mail address: trchen@mail.npue.edu.tw

Chart 1. Molecular structures of complexes **1**–**9**.

L 1 and **D1**: $R_1 = R_2 = R_3 = Y = H$ **L 2** and **D2**: $R_1 = R_3 = Y = H$, $R_2 = Cl$

L 3 and **D3**: $R_1 = R_2 = R_3 = H$, $Y = Cl$ **L 4** and **D4**: $R_2 = Y = H$, $R_1 = R_3 = F$

L 5 and **D5**: $R_1 = Y = H$, R_2-$R_3 = $ ⌬   **1**: $R_1 = R_2 = R_3 = Y = H$, $R' = CH_3$

2: $R_1 = R_3 = Y = H$, $R_2 = Cl$, $R' = CH_3$ **3**: $R_1 = R_3 = R_2 = H$, $Y = Cl$, $R' = CH_3$

4: $R_2 = Y = H$, $R_1 = R_3 = F$, $R' = CH_3$ **5**: $R_1 = Y = H$, R_2-$R_3 = $ ⌬, $R' = CH_3$

6: $R_1 = R_3 = Y = H$, $R_2 = Cl$, $R' = C_6H_5$ **7**: $R_2 = Y = H$, $R_1 = R_3 = F$, $R' = C_6H_5$

8: $R_1 = Y = H$, R_2-$R_3 = $ ⌬, $R' = C_6H_5$ **9**: $R_2 = Y = H$, $R_1 = R_3 = F$, $R' = CF_3$

Scheme 1. Synthesis of iridium complexes.

derivative ligands including 2-Phenylbenzoxazole (pbo) (**L1**), 2-(4-Chlorophenyl)benzoxazole (cpbo) (**L2**), 2-Phenyl-5-chlorobenzoxazole (pcbo) (**L3**), 2-(3,5-difluorophenyl)benzoxazole (fpbo) (**L4**), and 2-(2-Naphthyl)benzoxazole (nbo) (**L5**) were obtained and characterized. The cyclometalated Ir(III) chloro-bridged dimers having a general formula $(C^{\wedge}N)_2Ir(\mu\text{-}Cl_2)Ir(C^{\wedge}N)_2$ (**D1**–**D5**) were synthesized by the method reported by Nonoyama [1]. Except for the **D1** ((pbo)$_2$Ir(μ-Cl$_2$)Ir(pbo)$_2$), too unstable to be purified, the other chloro-bridged dimers (cpbo)$_2$Ir(μ-Cl$_2$)Ir(cpbo)$_2$ (**D2**),

(pcbo)$_2$Ir(μ-Cl)$_2$Ir(pcbo)$_2$ (**D3**), (dfpbo)$_2$Ir(μ-Cl)$_2$Ir(dfpbo)$_2$ (**D4**), and (nbo)$_2$Ir(μ-Cl)$_2$Ir(nbo)$_2$ (**D5**) were isolated and characterized by ^{1}H NMR, ^{13}C NMR, FAB-MS spectrometry, and elemental analyses. The desired iridium complexes (**1**–**9**) were synthesized by the reaction of cyclometalated Ir(III) chloro-bridged dimers with an appropriate ancillary ligand, acetylacetonate (acac), dibenzoyl-methanate (dbm), or 1,1,1,5,5,5-hexafluoroacetylacetonate (hfa-cac); all of the iridium complexes were purified and identified by ^{1}H NMR, ^{13}C NMR, elemental analyses, and FAB-MS spectrometry;

and further, complexes **3**, **4**, and **7–9** were characterized by a single-crystal X-ray analysis.

2.2. Structures of **3**, **4**, **7**, **8**, and **9**

The crystallographic data for all the structures reported here have been deposited in the Cambridge Database. Single-crystal structures of complexes **3**, **4**, **7**, **8**, and **9** are represented with ORTEP diagrams in Fig. 1. All the crystals were obtained from a mixed solution of dichloromethane and *n*-hexane. Complexes **3**, **4**, **7**, **8**, and **9** belong to the monoclinic space group *C*2/*c*, the monoclinic space group *P*2₁/*c*, the triclinic space group *P*1̄, the triclinic space group *P*1̄, and the monoclinic space group *P*2₁/*c*, respectively. The diversity of space groups for this series of complexes suggests that the packing of these complexes is very sensitive to the different substituents of the ligands [2a]. As depicted in Fig. 1, these five
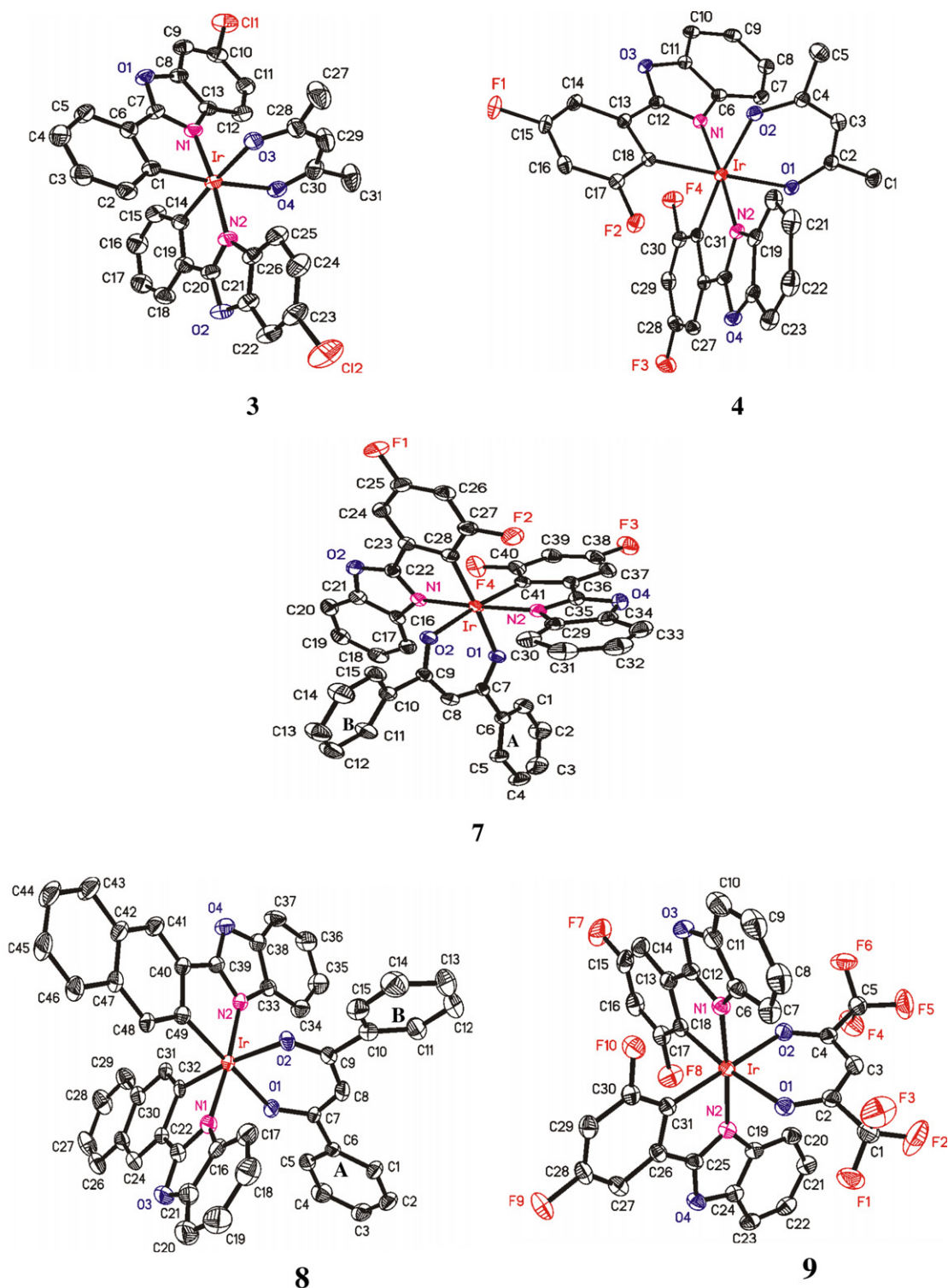

Fig. 1. ORTEP diagrams of **3**, **4**, **7**, **8**, and **9** with thermal ellipsoids drawn at 30% probability level. The hydrogen atoms have been omitted for clarity.

complexes adopt a distorted-octahedral coordination geometry around iridium, consisting of two benzoxazolate ligands and one β-diketonate ligand. Because of the smaller bite angles for the 2-aryl benzoxazolate chelating interaction, the crystal structures of these complexes are distorted octahedrons and prefer the *cis*-C–C, *trans*-N–N, and *cis*-O–O chelate disposition.

The selected bond distances and angles of complex **3**, **4**, **7**, and **9** are listed in Table 2, which shows that the bond length of the Ir–C bond in complex **3** (Ir–C_{av} = 2.005(4) Å) is shorter than those in complexes **4** (Ir–C_{av} = 2.029(4) Å), **7** (Ir–C_{av} = 2.021(5) Å), and **9** (Ir–C_{av} = 2.025(3) Å) because complex **3** has a stronger donating and back bonding interaction between aryl fragments of pcb and the iridium atom. Fig. 2a shows that the molecules of complex **3** are interlinked to form a one-dimensional linear structure through Cl···H interaction (Cl···H = 2.702 Å) in the packing diagram, and then, through C–H···O interaction (O···H = 2.424 Å), two linear chains are interlinked to form a self-complementary double chain, Fig. 2b [16]. In the self-complementary double chain, a valid stacking interaction between phenyl moiety and benzoxazole moiety of pcb is observed, in which the stacking distance (h) is 3.38 Å, the ring shift (r) is 1.46 Å, the inclination (θ) is 3.7°, and the direction angle (Ψ) is 66.7°, respectively [17]. Because the phenyl fragments of pcb carry a formal negative charge, the highest occupied molecular orbital (HOMO) is principally composed of the π orbital of the phenyl moiety of pcb, whereas the benzoxazolate fragment of pcb is formally neutral and is the principal contributor to the lowest unoccupied molecular orbital (LUMO) [18]. That is to say, the self-complementary double chain in the packing diagram of complex **3** is not only stabilized by the C–H···O interaction but also by the π–π* interaction between the HOMO (π) the LUMO (π*). Interestingly, the self-complementary double chain exhibits a helical structure, Fig. 2c. These phenomena reveal that complex **3**

Table 1
Crystal data for complexes **3**, **4**, **7**, **8**, and **9**

	Ir(P5CBO)$_2$(PDO)	Ir(FPBO)$_2$(PDO)	Ir(FPBO)$_2$(DBM)	Ir(NBO)$_2$(DBM)	Ir(FPBO)$_2$(HFPDO)
Empirical formula	$C_{34}H_{28}Cl_2IrN_2O_4$	$C_{31}H_{19}F_4IrN_2O_4$	$C_{41.50}H_{24}ClF_4IrN_2O_4$	$C_{52}H_{38}IrN_2O_4$	$C_{31}H_{13}F_{10}IrN_2O_4$
Fw	791.68	751.68	918.28	947.04	859.63
Temperature (K)	297(2)	297(2)	297(2)	297(2)	295(2)
Radiated used (λ[Å])	0.71073	0.71073	0.71073	0.71073	0.71073
Crystal size (mm^3)	0.46 × 0.17 × 0.16	0.38 × 0.36 × 0.35	0.60 × 0.44 × 0.25	0.58 × 0.50 × 0.44	0.46 × 0.35 × 0.24
Crystal system	monoclinic	monoclinic	triclinic	triclinic	monoclinic
Space group	C2/c	P2$_1$/c	P$\bar{1}$	P$\bar{1}$	P2$_1$/c
a (Å)	23.7943(15)	16.7347(16)	12.1208(15)	12.366(5)	17.5756(12)
b (Å)	12.9749(8)	18.2736(17)	12.8648(16)	13.553(6)	18.7959(14)
c (Å)	22.1626(14)	8.8533(8)	13.1540(17)	14.406(6)	8.8512(6)
α (°)	90	90	95.468(3)	93.145(8)	90
β (°)	112.9200(10)	100.711(2)	114.883(2)	109.520(7)	100.6360(10)
γ (°)	90	90	98.239(2)	113.283(7)	90
V (Å^3), Z	6302.0(7), 8	2660.2(4), 4	1813.6(4), 2	2041.0(15), 2	2873.8(3), 4
$\rho_{calc.}$ (g cm^{-3})	1.669	1.877	1.682	1.541	1.987
μ (mm^{-1})	4.447	5.089	3.821	3.321	4.753
F(000)	3112	1456	898	946	1648
Scan range θ (°)	2.13–26.02	2.23–26.02	1.73–26.15	1.93–26.19	2.17–26.01
Number of total reflections	17592	14750	10245	11426	15924
Number of unique reflections (R_{int})	6183 (0.0283)	5223 (0.0255)	7078 (0.0201)	7896 (0.0605)	5638 (0.0257)
Number of data/restraints/parameters	6183/2/388	5223/0/379	7078/0/496	7896/2/532	5638/0/487
Goodness-of-fit on F^2	0.986	1.002	1.136	1.265	1.143
R_1, wR_2 [$I > \sigma 2(I)$]	0.0277 and 0.0697	0.0244 and 0.0671	0.0318 and 0.0995	0.0595 and 0.1731	0.0212 and 0.0482
R_1, wR_2 (all data)	0.0427 and 0.0787	0.0296 and 0.0696	0.0352 and 0.1020	0.0627 and 0.1767	0.0258 and 0.0496

Table 2
Selected bond distance (Å) and bond angles for complexes **3**, **4**, **7**, **8**, and **9**

| Complex	Ir–C (Å)	Ir–O (Å)	Ir–N (Å)	N–Ir–N (°)	C–Ir–C (°)	O–Ir–O (°)	C–Ir–N (°)	N–Ir–O (°)	C–Ir–O (°)
3	2.006(4)	2.144(3)	2.037(3)	174.18(13)	91.13(17)	87.69(12)	96.01(15)	95.57(12)	175.62(14)
	2.005(4)	2.141(3)	2.033(3)				95.77(15)	94.38(12)	173.82(14)
							80.08(15)	89.85(12)	91.81(15)
							79.92(15)	88.60(12)	89.78(14)
4	2.030(3)	2.124(3)	2.053(3)	174.88(11)	91.47(14)	89.07(12)	99.80(13)	95.62(11)	174.63(12)
	2.028(4)	2.120(3)	2.033(3)				95.44(13)	94.03(12)	173.03(12)
							80.04(13)	89.48(11)	92.73(13)
							79.45(13)	86.44(12)	87.24(13)
7	2.031(5)	2.125(3)	2.028(4)	176.84(12)	93.56(18)	89.77(12)	98.29(18)	95.87(14)	175.16(14)
	2.011(5)	2.095(3)	2.026(4)				97.82(17)	95.54(15)	174.40(14)
							79.84(18)	86.60(14)	90.61(15)
							79.67(18)	86.46(14)	86.39(15)
8	2.023(7)	2.135(5)	2.070(6)	174.6(2)	91.3(3)	88.2(2)	97.3(3)	96.9(2)	176.2(2)
	1.986(6)	2.122(5)	2.034(6)				94.8(3)	96.9(2)	173.7(2)
							80.6(3)	87.6(2)	94.4(3)
							79.9(3)	86.3(2)	86.2(2)
9	2.030(3)	2.150(2)	2.061(2)	174.96(9)	90.19(11)	88.04(8)	100.41(11)	97.02(9)	175.30(9)
	2.019(3)	2.139(2)	2.035(2)				95.29(11)	95.17(9)	173.00(10)
							79.62(11)	88.02(9)	94.97(10)
							79.67(11)	85.19(9)	87.12(10)
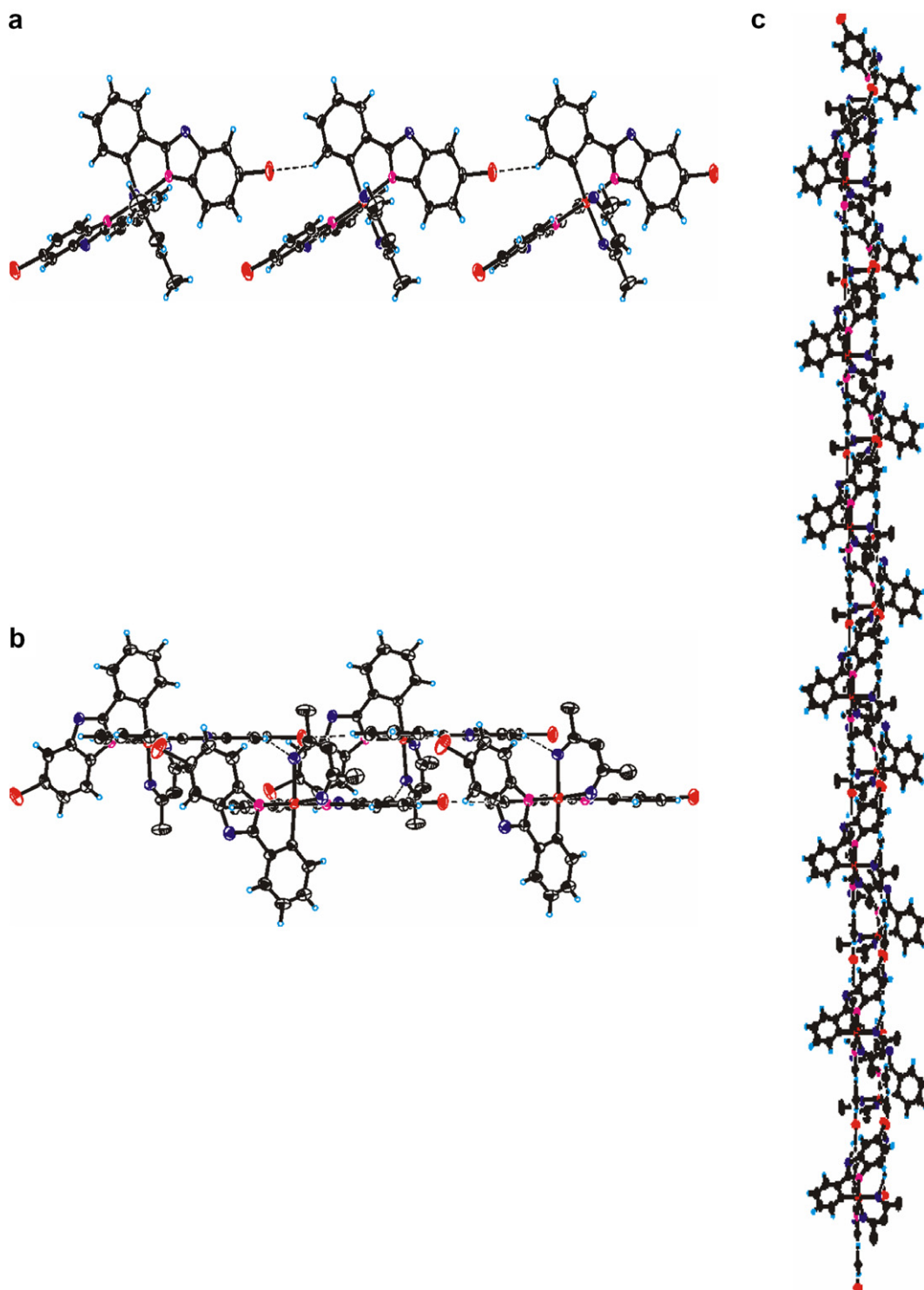
Fig. 2. The diagrams of **3** showing the linear molecular chain linked by the C–H···Cl interaction (a), the self-complementary double chain constructed by the C–H···O hydrogen bonds (b), and the helical structure built up by the C–H···Cl interaction, C–H···O hydrogen bonds, and the π–π^* interaction (c), respectively.

could be self-organized and sensitive to polar surroundings, which also suggests that this complex could be a promising material used as intrinsic or extrinsic fluorescent probes in the biophysical studies of the polarity of the microenvironment of peptides, proteins and lipid bilayers [19]. A detailed study of these properties is currently underway and will be presented in a future report.

Fig. 3a shows the most positive (or acidic) hydrogen atom of a dfpbo ligand in complex **4**, H_9, is interacting with the fluorine atom of the other dfpbo ligand to form a one-dimensional linear structure (F···H = 2.500 Å). Table 2 shows that the bond length of Ir–O of complex **4** is shorter (2.122 (3) Å) than that of complex **3** (2.143(3) Å), which implies that the negative charge on the oxygen atoms of the acac ligand in complex **4** is more delocalized into the iridium ion than that in complex **3**; hence, the charge on the oxygen atoms needed for the intermolecular interaction between the oxygen atom and the hydrogen atom is weakened. Therefore, the
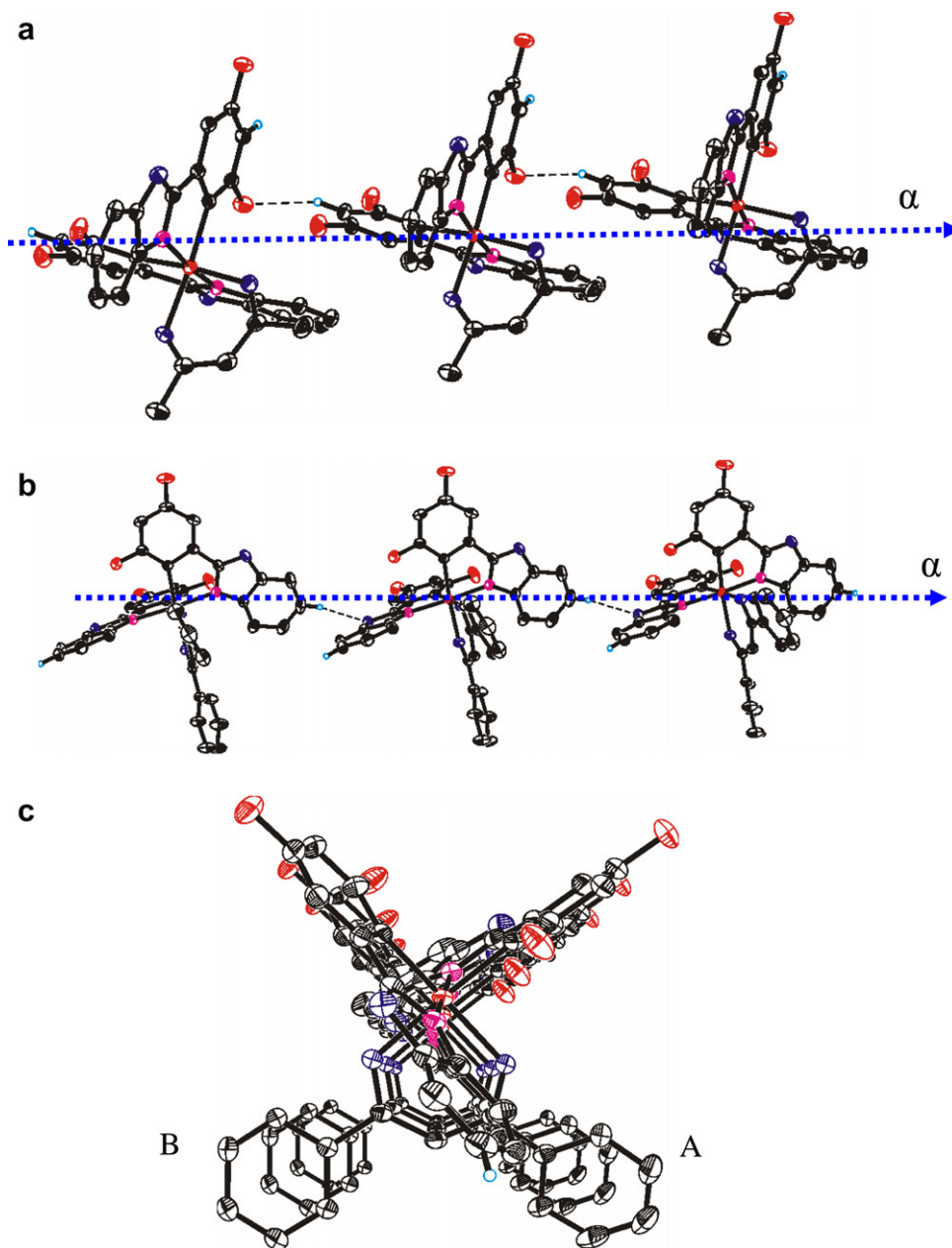
Fig. 3. (a) A packing diagram showing the linear chain of **4** linked by the C–H···F hydrogen bonds. A pseudo-axis (α) of the linear chain is designated to analyze this packing diagram. (b) A packing diagram showing the linear chain of **7** linked by the C–H···O hydrogen bonds. A pseudo-axis (α) of the linear chain is also designated. (c) A diagram showing the projection of the linear packing diagram of **7** visualized by an end-on view of the pseudo-axis (α).

C–H···O interaction has not been observed in the packing diagram of complex **4**, and then the self-complementary double chain has not been observed in complex **4**. The stacking parameters of the packing diagram of **4** (h = 3.39 Å, r = 1.67 Å, θ = 3.4°, Ψ = 63.7°) show that the π–π^* interaction between the HOMO on the difluorophenyl ring and the LUMO on the benzoxazole moiety of dfpbo of **4** is weaker than that of the corresponding interaction of complex **3** [17].

In Fig. 3b, the complex **7** molecules are also interlinked to form a one-dimensional linear structure but this packing diagram is quite different from that of complex **4**. To analyze these packing diagrams, the pseudo-axes (α) of the linear chains are designated in Fig. 3a and b. The linear chain in the packing diagram of complex **4** is built up by the H···F interlinking resulting from the interaction between an axial hydrogen atom of a dfpbo ligand and an equato-

rial fluorine atom of the other dfpbo ligand, whereas the linear chain in the packing diagram of complex **7** is constructed through the O···H interaction between an equatorial hydrogen atom of a dfpbo ligand and an equatorial oxygen atom of the other dfpbo ligand (O···H = 2.524 Å).

A projection of the linear packing diagram of **7** visualized by an end-on view of the pseudo-axis (α) (Fig. 3c) shows that there are two different sets of phenyl groups of dbm in the packing diagram designated as sets A and B, in which the dihedral angle between the phenyl ring of set A and the six-membered β-diketonate chelate ring is 15° and the dihedral angle between the phenyl ring of set B and the six-membered β-diketonate chelate ring is 24.7°, i.e. the phenyl rings of set A are sterically different from the phenyl rings of set B in the packing diagram of **7**. And because of the different steric effect of phenyl rings, the bond

length of Ir–O$_1$ (2.095(3) Å) is distinct from that of Ir–O$_2$ (2.125(3) Å); and further, by the trans influence, the bond length of Ir–C$_{28}$ (2.031(5) Å) is found to be longer than that of Ir–C$_{41}$ (2.011(5) Å). These data suggest that, for complex **7**, the conformation of the lumophore, composed of two dfpbo ligands and the central metal, iridium, can be affected by the steric effect of phenyl rings of the dbm ligand. Fig. 4 shows the ^{1}H NMR spectrum of complex **7** at various temperatures in acetone-d_6, in which the chemical shift of the protons (H$_a$) on the phenyl groups of dfpbo ligands are further deshielded at lower temperature, whereas the chemical shift of the protons (H$_b$) on the benzoxazole groups of the dfpbo ligands are further shielded as the temperature is lowered. This result indicates that for complex **7**, the variation of temperature gives rise to a variation of

the electron density on the phenyl and benzoxazole group of the dfpbo ligand. Because this phenomenon is not obviously observed for complex **4**, the temperature-dependent chemical shift must be due to the effect of the ancillary ligand. On the other hand, the conformation of the lumophore of complex **7** could be perturbed by the variation of temperature, and would be more sensitive to temperature than is the corresponding complex, **4**, having the same cyclometalated ligands (fpbo) as complex **7** but with a different ancillary ligand (acac). The integration ratio of the intensity of photoluminescence at low temperature (I_{77K}) to that at room temperature (I_{RT}) for complex **7** is much larger ($I_{77K}/I_{RT} = 12.96$) than that for complex **4** ($I_{77K}/I_{RT} = 0.78$), which proves that the lumophore of complex **7** is much more sensitive to temperature than for complex **4**.
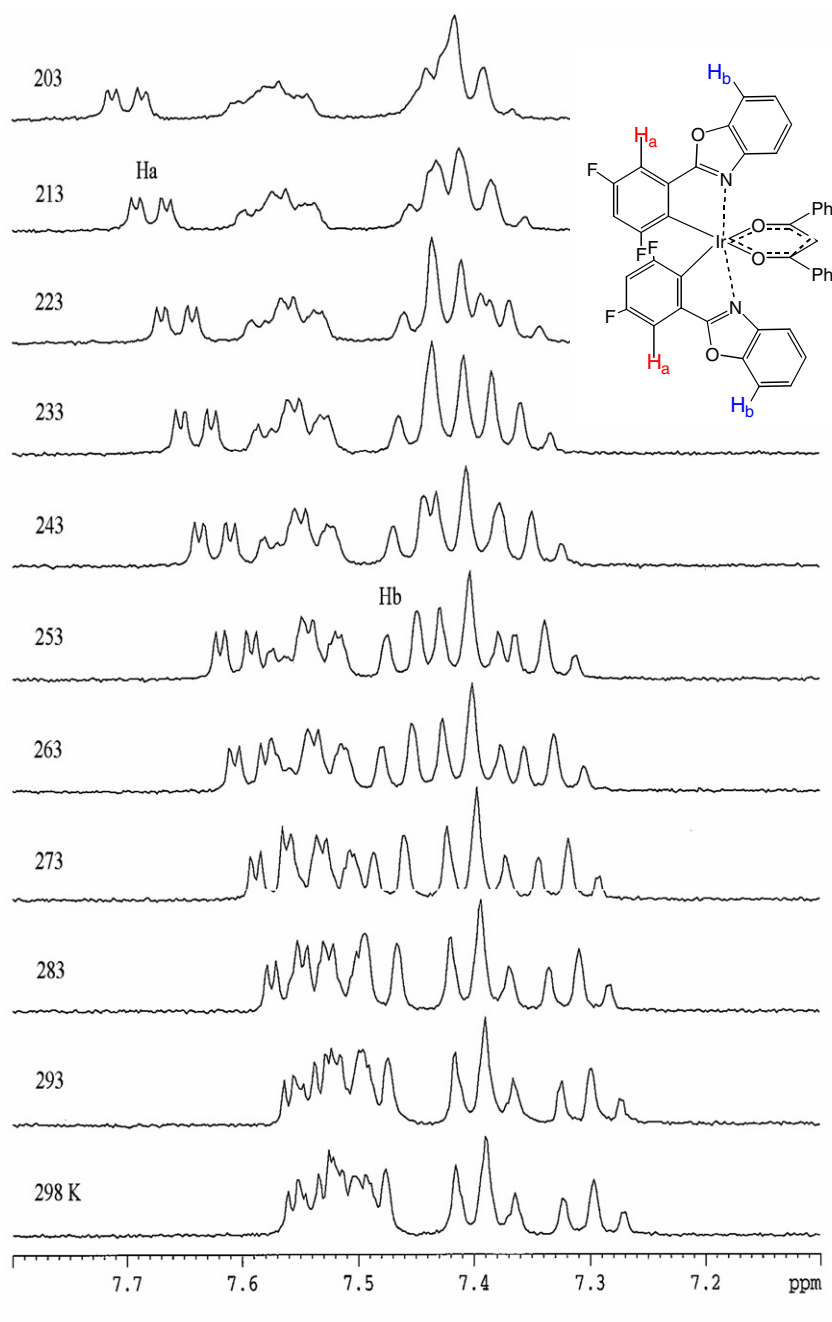

Fig. 4. An ^{1}H NMR spectrum of complex **7** at various temperatures.

Complex **8** possesses a similar packing diagram and the same space group as complex **7**. As depicted in Fig. 1 and Table 2, the dihedral angle between the phenyl ring of set A and the six-membered β-diketonate chelate ring (15.2°) is also obviously different from that between the phenyl ring of set B and the six-membered β-diketonate chelate ring (24.6°); and the bond length of Ir–C$_{49}$ (2.032 (7) Å) is also distinct from that of Ir–C$_{32}$ (1.986 (6) Å). The integration ratio of the intensity of photoluminescence at different temperature for complex **8** is also quite larger (I_{77K}/I_{RT} = 7.03) than that for complex **5** (I_{77K}/I_{RT} = 0.73), which is composed of the same C^N ligand (nbo) as complex **8** but has a different ancillary ligand. These data reveal that the conformation of the lumophore of complex **8** is also more sensitive to temperature than for complex **5**.

2.3. Electrochemical properties

The electrochemical properties of **1–9** in CH$_2$Cl$_2$ are summarized in Table 3. All complexes show reversible oxidation waves (see Fig. 5) in the range of 0.45–1.07 V versus ferrocene/ferrocenium. The HOMO and LUMO levels of all complexes were calculated according to the equation HOMO/LUMO (eV) = −(4.8 + E_{onset}) [1]. When an electron-withdrawing group such as F or Cl was introduced into the cyclometalating ligand, the $E_{1/2(ox)}$ of Ir(III) complexes shifted more positively than the $E_{1/2(red)}$ does, which leads to an increase of energy gap between the HOMO and LUMO levels. For complexes with the same C^N cyclometalated ligands, the oxidation potentials of (C^N)$_2$Ir(dbm) complexes are similar to those of (C^N)$_2$Ir(acac) complexes, but the complexes containing

dbm as an ancillary ligand display higher reduction potentials than do the complexes containing acac ligand, which indicates that the frontier molecular orbitals are affected by the phenyl groups of dbm in the (C^N)$_2$Ir(dbm) complexes, and these experimental data concur with a theoretical study: the HOMOs of the (C^N)$_2$Ir(dbm) and (C^N)$_2$Ir(acac) complexes are both composed of d(Ir) and π(C^N), whereas the LUMO is only localized on the π*(C^N) orbital for (C^N)$_2$Ir(acac) complexes and is composed of π*(C^N) and π*(dbm) for (C^N)$_2$Ir(dbm) complexes; therefore the LUMO orbital of (C^N)$_2$Ir(dbm) complexes can be affected by the ancillary ligand, dbm [20].

2.4. Photophysical properties

The absorption and photoluminescence spectra of complexes **1–9** in CH$_2$Cl$_2$ solutions are depicted in Figs. 6 and 7; the photophysical data of all the iridium complexes reported here are summarized in Tables 3 and 4. The strong absorption bands in the ultraviolet region at about 240–310 nm with high extinction coefficients ($\varepsilon > 4.0 \times 10^4$ cm^{-1} M^{-1}) are assigned to the ligand localized π–π* transitions by the comparison with the absorption spectra of the corresponding C^N ligands. The intense absorption bands at lower energy (320–420 nm, ε = 5000–25 000 cm^{-1} M^{-1}) can be assigned to the typical spin-allowed metal to ligand charge-transfer (^{1}MLCT) transitions; the weaker absorption bands at the still lower energy (413–475 nm, ε = 1300–5000 cm^{-1} M^{-1}) are assigned to the spin-forbidden metal to ligand charge-transfer (^{3}MLCT) transitions. The energies of these MLCT transitions are

Table 3
UV–Vis absorption and electrochemical properties of complexes **1–9**

Complex	Absorption[a] λ (nm) {ε, 10^4 cm^{-1} M^{-1}}	$E_{1/2}^{ox}$ (V)	$E_{1/2}^{red}$ (V)	$\Delta E_{1/2}$ (V)	HOMO (eV)	LUMO (eV)	E_{1MLCT}[a] (V)
1	262 (4.12), 295 (2.1), 338 (0.49), 370 (0.25), 416 (0.17), 443 (0.13)	0.45	−2.30	2.75	−5.25	−2.50	2.98
2	255 (4.11), 300 (4.26), 336 (1.14), 379 (0.73), 410 (0.50), 445 (0.40)	0.70	−2.11	2.81	−5.50	−2.69	3.02
3	258 (4.09), 298 (4.10), 338 (1.16), 379 (0.76), 409 (0.53), 440 (0.40)	0.73	−2.32	3.05	−5.53	−2.48	3.03
4	250 (4.00), 299 (3.84), 338 (1.55), 420 (0.70), 445 (0.35), 505 (0.031)	0.78	−2.13	2.91	−5.50	−2.67	2.95
5	245(5.58), 310 (5.88), 360 (1.81), 408 (0.56), 475 (0.32)	0.55	−2.08	2.63	−5.35	−2.72	2.61
6	258 (3.58), 300 (3.73), 334 (1.5), 379 (0.99), 416 (0.6), 439 (0.38)	0.73	−2.13	2.86	−5.53	−2.67	2.98
7	255 (4.68), 299 (4.7), 334 (2.25), 413 (0.94), 445 (0.44), 502 (0.05)	0.78	−2.04	2.82	−5.58	−2.76	2.78
8	245 (5.10), 303 (5.64), 364 (2.44), 406 (1.20), 453 (0.48)	0.54	−1.99	2.53	−5.34	−2.81	2.74
9	248 (3.17), 296 (3.51), 326 (1.99), 413 (0.57), 504 (0.035)	1.07	−2.12	3.19	−5.87	−2.68	3.00

[a] Estimated from the ^{1}MLCT absorption bands, $E_{1MLCT}(eV) = \frac{hc}{\lambda_{1MLCT}}$, (h: Planck's constant, c: velocity of light in vacuum).

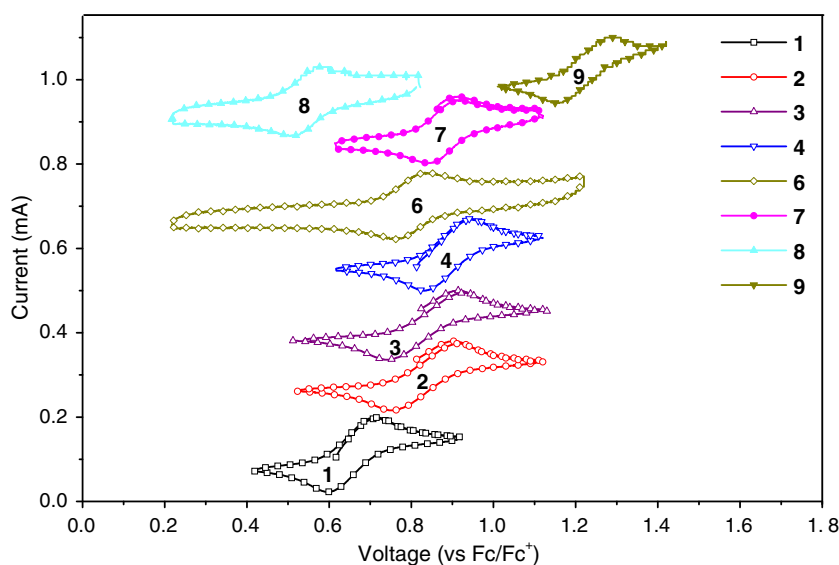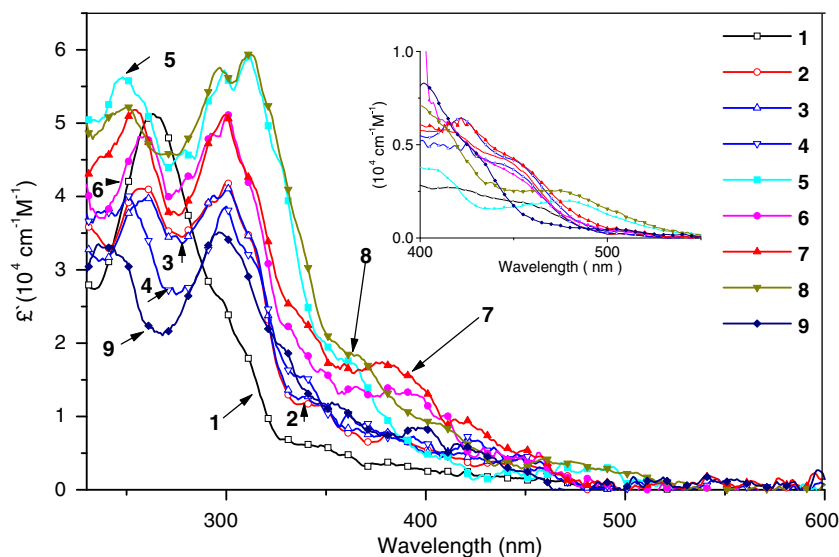**Fig. 5.** Cyclic voltammograms of **1–9**, measured in CH$_2$Cl$_2$.

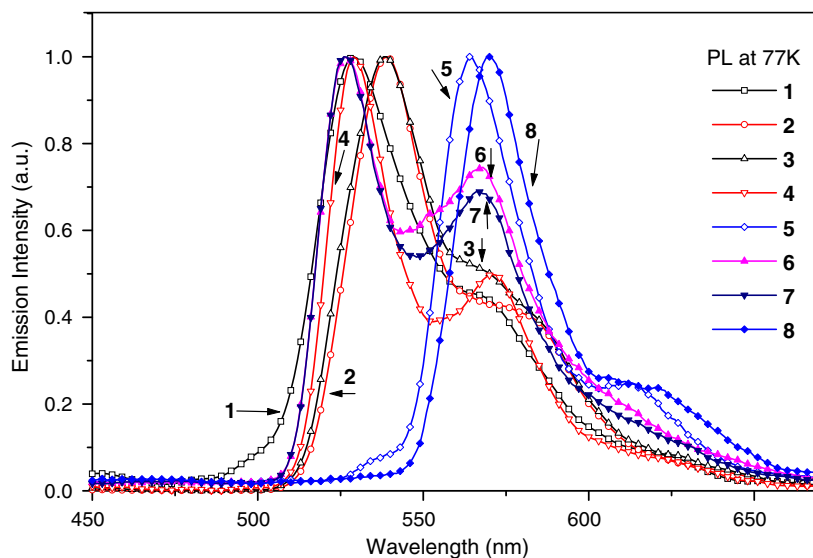**Fig. 6.** Room-temperature absorption spectra of **1–9**, measured in CH_2Cl_2.

Fig. 7. Emission spectra of **1–9** at 77 K in CH_2Cl_2.

only weakly solvatochromic, undergoing a blue-shift in a polar (acetonitrile) solvent, which indicates that the polarity of the ground state is higher than that of the excited state for the complexes reported here. The much weaker, lowest energy absorption bands (505–515 nm, $\varepsilon = 40$–500 cm^{-1} M^{-1}) can be identified as a triplet transition (T_1) on the basis of the small energy shift (350–900 cm^{-1}) between absorption and emission at room temperature.

As shown in Table 4, the photoluminescence of all complexes are sensitive to oxygen, which indicates that the emitting states of these complexes have triplet character [1]. Two prominent vibronic features are present in the emission spectra (Fig. 7) and the Huang–Rhys factor, S_M value, can be estimated from the intensity ratio of this first major vibrational transition to the highest energy peak [21]. The S_M value is a measure of vibronic coupling between the ground and the excited state and is proportional to the degree of structural distortion that occurs in the excited state relative to the ground state and can quantify the degree of electron-vibrations coupling [7]. A large S_M value indicates a strong coupling between

the dominant ligand-localized vibrations in the excited state and the ground state, and this explanation also suggests that the increment of the S_M value indicates less ^1MLCT character in the T_1 state [7].

Table 4 shows that, at 77 K, complexes including dbm as an ancillary ligand have a larger S_M value than do the complexes containing acac as an ancillary ligand, which indicates that the T_1 state of complexes possessing dbm ligand become more ligand-localized (^3LC) in character (less ^1MLCT character in the T_1 state). Therefore, the decreased ^1MLCT admixture leads to the decrease in quantum yield of $(C^\wedge N)_2Ir(dbm)$ complexes (Φ is in a lower range between 0.0015 and 0.0045 for $(C^\wedge N)_2Ir(dbm)$ complexes and in a higher range between 0.02 and 0.15 for $(C^\wedge N)_2Ir(acac)$ complexes). Interestingly, the Huang–Rhys factor of the complexes containing dbm as an ancillary ligand increases with increasing temperature (Fig. 8), which indicates that the emitting states of this kind of complex have more ^3LC character with increasing temperature, and therefore the quantum yield is decreased. As described above,

Table 4
Photophysical properties of complexes **1**–**8**

Complex	Emission at RT					Emission at 77 K[b]			
	$\lambda_{max}{}^a$, $\lambda_{max}{}^b$ (nm)	τ^a,τ^b (μs)	Φ^a,Φ^b	$k_r{}^a$, $k_r{}^b$ (10^5 s^{-1})	$k_{nr}{}^a$, $k_{nr}{}^b$ (10^6 s^{-1})	λ_{max} (nm)	E_{em} (0–0) (10^4 cm^{-1})	$\hbar\omega_M$ (cm^{-1})^e	S_M
1	531	1.30	0.07	0.54	0.72	529	1.89	1360	0.45
	530								
2	530	1.10	0.12	1.09	0.80	528	1.86	1341	0.53
	531	0.14	0.04	2.86	6.86				
3	537	1.41	0.13	0.92	0.62	538	1.86	1074	050
	530	0.65	0.06	0.92	1.45				
4	530	0.84	0.15	1.79	1.01	529	1.89	1421	0.42
	530	0.30	0.05	1.67	3.17				
5	568	0.95	0.02	0.21	1.03	565	1.77	1538	0.22
	566								
6	528	1.03	0.0045	0.04	0.97	527	1.90	1401	0.60
	529								
7	531	0.42	0.004	0.095	2.37	527	1.90	1401	0.58
	531								
8	579	0.81	0.0015	0.019	1.23	572	1.75	1388	0.24
	579								

[a] Measured in dichloromethane solution at a concentration of 1×10^{-6} M.
[b] Measured in acetonitrile solution at a concentration of 1×10^{-6} M. The emission energy, E_{em} (0–0), was obtained from the maximum emission wavelength and the energy of $\hbar\omega_M$ was obtained from the energy difference (in cm^{-1}) of the first two emission spectra. The Huang–Rhys factor, S_M value, was estimated from the intensity ratio of the first major vibrational transition to the highest energy peak at the 77 K emission spectra.
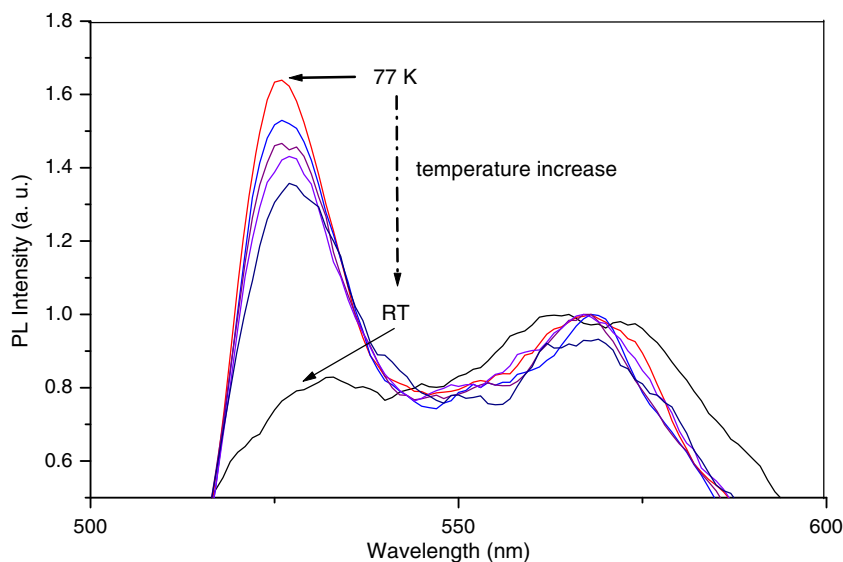

Fig. 8. Emission spectra of complex **7** at various temperatures.

the emission intensities of complex **7** and **8** are sensitive to temperature. A resembling phenomenon is also observed in the comparison between complex **6** and complex **2** (I_{77K}/I_{RT} is 9.27 for complex **6** and 1.17 for complex **2**, respectively).

For luminescent molecules, the quantum yield of emission (Φ) is generally given by

$$\Phi = k_r\tau$$

where k_r is the rate constant for radiative decay, and τ is the measured experimental lifetime of the emitting state [22]. Experimentally, when the quantum yield has been determined, the radiative decay rate (k_r) and the nonradiative decay rate (k_{nr}) are given by [7]

$$k_r = \frac{\Phi}{\tau}, \text{ and } k_{nr} = \frac{(1-\Phi)}{\tau}$$

The lifetime, k_r, and k_{nr} values of complexes **1**–**8** have been obtained and listed in Table 4; all of the (C$^\wedge$N)$_2$Ir(LL′) complexes have short luminescence lifetime (τ = 0.3–2 μs) at room temperature. The radiative decay rates of the (C$^\wedge$N)$_2$Ir(LL′) complexes range between 2.0×10^3 and 3.0×10^5 s^{-1}. The nonradiative decay rates span a narrower range of values (5.0×10^5 to 7.0×10^6 s^{-1}). As shown in Table 4, the k_r values of (C$^\wedge$N)$_2$Ir(acac) complexes are more than ten times as large as those of (C$^\wedge$N)$_2$Ir(dbm) complexes, which indicates that the higher quantum yield of (C$^\wedge$N)$_2$Ir(acac) complexes is due to the higher k_r values.

Furthermore, the radiative decay rate can be evaluated by

$$k_r = \frac{4E_{em}^3}{3h} |\langle\psi_e | \vec{d} | \psi_g\rangle|^2$$

where E_{em} is the emission energy and $|<\psi_e | \vec{d} | \psi_g>|^2$ describes the probability for an excited to ground state transition. Because the emission energies of (C$^\wedge$N)$_2$Ir(acac) complexes are not obviously different from those of the corresponding (C$^\wedge$N)$_2$Ir(dbm) complexes, the variations in the radiative decay rate of (C$^\wedge$N)$_2$Ir(LL′) complexes are mostly due the change of the transition probability, $|<\psi_e | \vec{d} | \psi_g>|^2$; in other words, the transition probabilities of
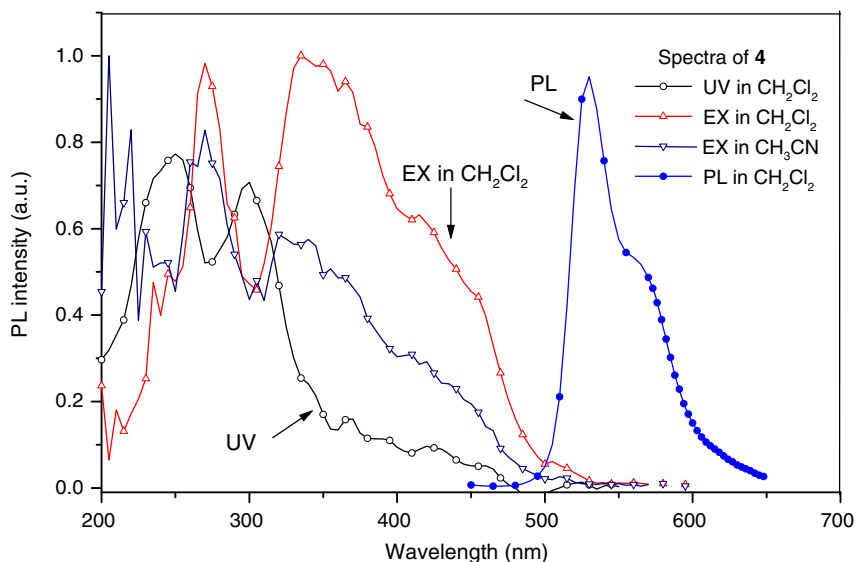
Fig. 9. Absorption (UV), excitation (EX), and emission (PL) spectra of complex **4** at room-temperature.

$(C^\wedge N)_2$Ir(acac) complexes must be higher than that of $(C^\wedge N)_2$Ir(dbm) complexes.

As described in Table 4, the quantum efficiencies of all complexes reported here are obviously reduced when a polar solvent is used. Sajoto et al. have reported that the decline in quantum efficiencies of some iridium complexes is due to a significant decrease in the radiative rates, which comes about from an increased separation between the MLCT and LC energies as a result of the decreased HOMO energy [18]. For the iridium complexes reported here, their radiative rates (k_r) and E_{em} are not obviously changed in different solvent so that the decrease in quantum efficiencies could not be attributed to the decrease of radiative rate or the increase of emission energy. Tamayo et al. reported that because of the efficient intersystem crossing (ISC) between the singlet and triplet excited states brought about by the strong spin–orbit coupling of the Ir(III) metal ion, d^6 Ir(III) complex can exhibit long excited-state lifetime and high luminescence efficiencies [23], which implies that the efficient ISC leads to the excited states possessing more triplet character, and hence, a longer lifetime, in which the vibrational perturbation $\{|<T_1^v|H_{so}|S_n>|$, where H_{so} is the spin–orbit coupling$\}$ is required for the effective mixing of singlet states with T_1 [22]. The excitation spectrum of complex **4**, Fig. 9, shows that the absorption band of MLCT transition contributes to a part of the photoluminescence in a polar solvent (acetonitrile) and this contribution is increased with decreasing polarity of solvent (dichloromethane), in which the vibrational structure can be observed in the excitation spectrum. Since the probability of $|<T_1^v|H_{so}|S_n>|$ increases with decreasing solvent polarity, the lower S_M values were observed in a low polar environment, which also implies that the T_1 states of complexes possess more ^{1}MLCT character in dichloromethane; therefore, a longer excited-state lifetime and a higher luminescence efficiency were observed in dichloromethane than that in acetonitrile.

3. Conclusion

This work reports detailed synthesis and characterization of nine $(C^\wedge N)_2$Ir(LL′) complexes composed of benzoxazole derivatives and β-diketonate ligands. The effects of $C^\wedge N$ cyclometalated ligands and β-diketonate ligands on the electrochemical and photophysical properties were studied. The ancillary ligands obviously affect the electrochemical, photophysical properties, the conformation of the

lumophore of complexes, and the sensitivities of complexes to temperature and solvent polarity. The excited states of complexes possessing dbm as an ancillary ligand become more ligand-localized than those containing acac do, and the less ^{1}MLCT character in the T_1 transition for $(C^\wedge N)_2$Ir(dbm) complexes leads to the decrease in radiative decay rate, the lifetime of excited states and the quantum efficiencies. The $(C^\wedge N)_2$Ir(acac) complexes reported here are highly emissive at room temperature and stable to air, humidity, and most organic solvents. Most of the complexes reported here could be promising materials used as biophysical preparations or electroluminescent materials.

4. Experimental

4.1. Materials and equipment

Acetylacetone and dibenzoylmethane were obtained from Alfa Aesar. 1,1,1,5,5,5-hexafluoroacetylacetone and 2,4-difluorobenzoic acid were purchased from Matrix, and $IrCl_3 \cdot nH_2O$ was from Seedchem Co. All other chemicals were purchased from Acros and used as received.

NMR spectra were measured on a Bruker Avance-400 MHz or a Mercury 300 MHz NMR spectrometer. UV–Vis spectra were obtained from a Cary 50 Probe spectrophotometer. Elemental analyses (CHN) were obtained from an Elementar vario EL III analyzer. Mass spectra were taken with a Finnigan/Thermo Quest MAT 95XL instrument with electron impact ionization for organic compounds or fast atom bombardment for metal complexes. Emission spectra were obtained from a Hitachi-F7000 spectrometer. The quantum efficiency (Φ_{PL}) was carried out at room temperature in dichloromethane solution. A solution of 10-methyl-9(10)-acridone in dichloromethane ($\Phi = 0.95$) was used as a reference. Phosphorescence lifetime measurements were performed on an Edinbrugh Instrument model OB920 spectrometer.

4.2. Electrochemical measurements

Cyclic voltammetry were performed using a CHI voltammetric analyzer. Anhydrous and nitrogen-purged CH_2Cl_2 was used as the solvent, and 0.1 M tetra(n-butyl)ammonium hexafluorophosphate ($Bu_4N^+ \cdot PF_6^-$) was used as the supporting electrolyte. A glassy-carbon rod was used as the working electrode, a platinum-wire

was used as the counter electrode, and a Ag/Ag+ electrode as the reference electrode. The redox potentials are based on values measured from differential pulsed voltammetry and are reported relative to a ferrocene/ferrocenium (Fc/Fc⁺) redox couple used as an internal standard [23].

4.3. Synthesis of benzoxazole derivative ligands (L1–L5)

The benzoxazole derivative ligands, L1–L5, were prepared by Philips' condensation (as shown in Scheme 1) as follows: [24] one equiv of benzoic acid (or substituted benzoic acid) and 1.05 equiv of an appropriate aminophenol were added to polyphosphoric acid (10 g/mmol of benzoic acid), and then the mixture was stirred at 200 °C for 5 hours. After cooling to room temperature, the mixture was slowly poured into pure water with well stirred; the precipitate was collected by filtration, washed with pure water (3 × 100 ml), and dried to yield a crude product. The crude product was purified by column chromatography over silica gel using n-hexane–CH_2Cl_2 (1:1–1:5) as eluent to obtain the corresponding ligand.

4.4. Synthesis of 2-phenylbenzoxazole (L1)

White crystal. 70% yield. ^{1}H NMR (300 MHz, CDCl$_3$, 298 K; δ (ppm)): 8.28–8.25 (m, 2H), 7.80–7.76 (m, 1H), 7.60–7.56 (m, 1H), 7.53–7.51 (m, 3H), 7.37–7.33 (m, 2H). ^{13}C NMR (75 MHz, CDCl$_3$, 298 K; δ (ppm)): δ163.2, 151.0, 142.3, 131.7, 129.1, 127.8, 127.4, 125.3, 124.8, 120.263, 110.8. Anal. calc. for C$_{13}$H$_9$NO (MW = 195.22): C, 79.98; H, 4.65; N, 7.18. Found: C, 79.99; H, 4.65; N, 7.20%. MS (FAB; m/z): 195.0686.

4.5. Synthesis of 2-(4-chlorophenyl)benzoxazole (L2)

White crystal. 55% yield. ^{1}H NMR (300 MHz, CDCl$_3$, 298 K; δ (ppm)): 8.17 (d, J = 8.7 Hz, 2H), 7.77–7.74 (m, 1H), 7.57–7.54 (m, 1H), 7.48 (d, J = 8.7 Hz, 2H), 7.38–7.33 (m, 2H). ^{13}C NMR (75 MHz, CDCl$_3$, 298 K; δ (ppm)): 162.2, 150.9, 142.2, 137.9, 129.4, 129.0, 125.8, 125.5, 124.9, 120.3, 110.8. Anal. calc. for C$_{13}$H$_8$ClNO (MW = 229.67): C, 67.98; H, 3.51; N, 6.10. Found: C, 67.98; H, 3.53; N, 6.11%. MS (FAB; m/z):229.0303.

4.6. Synthesis of 2-phenyl-5-chlorobenzoxazole (L3)

White crystal. 65% yield. ^{1}H NMR (300 MHz, CDCl$_3$, 298 K; δ (ppm)): 8.23–8.20 (m, 2H), 7.66 (d, J = 8.7 Hz, 1H), 7.58 (d, J = 1.8 Hz, 1H), 7.55–7.49 (m, 3H), 7.32 (dd, J = 8.7, 1.8 Hz, 1H). ^{13}C NMR (75 MHz, CDCl$_3$, 298 K; δ (ppm)): 163.9, 151.1, 141.1, 132.0, 130.9, 129.2, 127.8, 126.9, 125.5, 120.7, 111.4. Anal. calc. for C$_{13}$H$_8$ClNO (MW = 229.67): C, 67.98; H, 3.51; N, 6.10. Found: C, 67.91; H, 3.52; N, 6.10%. MS (FAB; m/z): 229.0300.

4.7. Synthesis of 2-(3,5-difluorophenyl)benzoxazole (L4)

White crystal. 85% yield. ^{1}H NMR (300 MHz, CDCl$_3$, 298 K; δ (ppm)): 7.80–7.74 (m, 3H), 7.59–7.56 (m, 1H), 7.41–7.36 (m, 2H), 7.00–6.96 (m, 1H). ^{13}C NMR (75 MHz, CDCl$_3$, 298 K; δ (ppm)): 165.1, 164.9, 161.8, 161.7, 160.9, 151.0, 141.9, 130.4, 130.3, 130.1, 126.1, 125.2, 120.6, 110.9, 110.8, 110.7, 110.6, 107.3, 107.0, 106.7. Anal. calc. for C$_{13}$H$_7$F$_2$NO (MW = 231.20): C, 67.53; H, 3.05; N, 6.06. Found: C, 67.50; H, 3.08; N, 5.99%. MS (FAB; m/z): 231.0496.

4.8. Synthesis of 2-(2-naphthyl)benzoxazole (L5)

White crystal. 65% yield. ^{1}H NMR (300 MHz, CDCl$_3$, 298 K; δ (ppm)): 8.76 (s, 1H), 8.31 (dd, J = 8.7, 1.8 Hz, 1H), 7.99–7.94 (m, 2H), 7.89–7.86 (m, 1H), 7.83–7.80 (m, 1H), 7.62–7.54 (m, 3H), 7.40–7.25 (m, 2H). ^{13}C NMR (75 MHz, CDCl$_3$, 298 K; δ (ppm)): 163.4, 151.1, 142.4, 134.9, 133.2, 129.1, 129.0, 128.3, 128.1, 128.0, 127.1, 125.4, 124.8, 124.6, 124.194, 120.2, 110.8. Anal. calc. for C$_{17}$H$_{11}$NO (MW = 245.28): C, 83.24; H, 4.52; N, 5.71. Found: C, 83.25; H, 4.57; N, 5.71%. MS (FAB; m/z): 245.0839.

4.9. Synthesis of cyclometalated Ir(III)μ-chloro-bridged dimers (D2–D5)

Cyclometalated Ir(III) chloro-bridged dimers (D2-D5) were synthesized according to previous papers (as shown in Scheme 1) [1–3]. A mixture of 2-ethoxyethanol and water (3:1, v/v) was added to a flask containing iridium trichloride (IrCl$_3$•3H$_2$O, 2 mmol) and an appropriate benzoxazole derivative (L2–L5, 5 mmol), and then the mixture was refluxed for 24 hours under nitrogen. After cooling to room temperature, the mixture was poured into 20 ml of pure water, and the dimer precipitate was filtered off, washed with deionized water, and followed by drying at 60 °C in a vacuum oven.

4.10. Synthesis of (cpbo)₂Ir(μ-Cl)₂Ir(cpbo)₂ (D2)

Yellow solid. 85% yield. ^{1}H NMR (300 MHz, DMSO-d^6, 298 K; δ (ppm)): 8.76–8.73 (m, 2H), 8.09–8.54 (m, 4H), 7.95 (d, J = 8.4 Hz, 2H), 7.84–7.60 (m, 8H), 7.48 (dd, J = 8.2, 2.1 Hz, 2H), 7.38 (t, J = 8.4 Hz, 2H), 7.14 (t, J = 8.4 Hz, 2H), 7.03 (dd, J = 8.1, 1.8 Hz, 2H), 6.40 (d, J = 7.8 Hz, 2H), 6.0 (d, J = 2.1 Hz, 2H). Anal. calc. for C$_{52}$H$_{28}$Cl$_6$Ir$_2$N$_4$O$_4$ (MW = 1369.98): C, 45.59; H, 2.06; N, 4.09. Found: C, 45.67; H, 2.10; N, 4.11%. MS (FAB; m/z): 1367.9515.

4.11. Synthesis of (pcbo)₂Ir(μ-Cl)₂Ir(pcbo)₂ (D3)

Yellow solid. 70% yield. ^{1}H NMR (300 MHz, DMSO-d^6, 298 K; δ (ppm)): 8.22 (d, J = 1.8 Hz, 4H), 7.65 (dd, J = 7.8, 1.2 Hz, 4H), 7.36 (d, J = 9 Hz, 4H), 7.1 (dd, J = 8.7, 2.1 Hz, 4H), 6.87 (dt, J = 7.4, 1.2 Hz, 4H), 6.68 (dt, J = 7.4, 1.2 Hz, 4H), 6.17 (d, J = 7.8 Hz, 4H). Anal. calc. for C$_{52}$H$_{28}$Cl$_6$Ir$_2$N$_4$O$_4$ (MW = 1369.98): C, 45.59; H, 2.06; N, 4.09. Found: C, 44.46; H, 2.10; N, 4.09%. MS (FAB; m/z): 1367.9504.

4.12. Synthesis of (fpbo)₂Ir(μ-Cl)₂Ir(fpbo)₂ (D4)

Dark yellow solid. 75% yield. ^{1}H NMR (300 MHz, DMSO-d^6, 298 K; δ (ppm)): 8.18 (d, J = 8.18, 8.1 Hz, 4H), 7.31 (dd, J = 7.6, 2.7 Hz, 4H), 7.22–7.12 (m, 8H), 6.99 (dt, J = 7.1, 1.5 Hz, 4H), 6.14 (dt, J = 9.6, 2.7 Hz, 4H). ^{13}C NMR (75 MHz, CDCl$_3$, 298 K; δ (ppm)): 174.9, 169.2, 169.1, 167.5, 167.4, 160.3, 160.2, 158.7, 158.6, 149.1, 140.8, 133.6, 133.5, 133.4, 133.3, 125.1, 124.4, 118.0, 115.3, 115.0, 110.9, 108.6, 108.4, 107.2, 107.0, 106.8, 31.8, 31.1, 22.8, 14.3. Anal. calc. for C$_{52}$H$_{24}$F$_8$Cl$_2$Ir$_2$N$_4$O$_4$ (MW = 1376.12): C, 45.38; H, 1.76; N, 4.07. Found: C, 44.89; H, 1.70; N, 3.98%. MS (FAB; m/z): 1376.0319.

4.13. Synthesis of (nbo)₂Ir(μ-Cl)₂Ir(nbo)₂ (D5)

Red solid. 65% yield. ^{1}H NMR (300 MHz, DMSO-d^6, 298 K; δ (ppm)): 8.93 (d, J = 8.4 Hz, 2H), 8.63 (s, 2H), 8.48 (s, 2H), 8.38 (s, 2H), 8.16 (d, J = 7.5 Hz, 2H), 8.11 (d, J = 7.2 Hz, 2H), 7.93 (d, J = 7.2 Hz, 2H), 7.83–7.80 (m, 4H), 7.71–7.57 (m, 8H), 7.37 (t, J = 7.8 Hz, 2H), 7.25–7.23 (m, 4H), 7.14 (t, J = 7.5 Hz, 2H), 7.02–7.0 (m, 2H), 6.5 (d, J = 7.5 Hz, 2H), 6.37 (s, 2H). Anal. calc. for C$_{68}$H$_{40}$Cl$_2$Ir$_2$N$_4$O$_4$ (MW = 1432.43): C, 57.02; H, 2.82; N, 3.91. Found: C, 56.28; H, 3.82; N, 2.85%. MS (FAB; m/z): 1432.1689.

4.14. Synthesis of iridium complexes 1–9

Complexes **1**–**9** were synthesized according to a method given previously in the literature (as shown in Scheme 1) [1]. One equiv of a cyclometalated Ir(III) chloro-bridged dimer [(C^N)$_2$Ir(μ-Cl$_2$)Ir(C^N)$_2$], 5 equiv of silver carbonate, and 2.5 equiv of an appropriate ancillary ligand were added to 2-ethoxyethanol (10 ml/mmol of Ir(III) chloro-bridged dimer), and then the mixture was stirred and refluxed under nitrogen for 24 hours. After that, the mixture was cooled to ambient temperature and concentrated under reduced pressure. The residue was taken up in dichloromethane, and the silver salt was removed by filtration through celite. The resultant solution was concentrated and further purified by column chromatography over silica gel using *n*-hexane–CH$_2$Cl$_2$ (1:1–1:9) as eluent to obtain the corresponding iridium complex. The iridium complexes were characterized by ^{1}H NMR, ^{13}C NMR, elemental analysis, and FAB-MS spectrometry. Moreover, complexes **3**, **4**, and **7**–**9** were further identified by a single-crystal X-ray analysis.

4.15. Synthesis of bis[2-phenylbenzoxazolato-N,C$^{2'}$]iridium(III) (acetylacetonate) (1)

Orange solid. 60% yield (based on the corresponding dimer). ^{1}H NMR (300 MHz, CDCl$_3$, 298 K; δ (ppm)): 7.69–7.65 (m, 4H), 7.56–7.53 (m, 2H), 7.47–7.39 (m, 4H), 6.90–6.85 (m, 2H), 6.75–6.70 (m, 2H), 6.51 (d, *J* = 7.5 Hz, 2H), 5.26 (s, 1H), 1.85 (s, 6H). ^{13}C NMR (75 MHz, CDCl$_3$, 298 K; δ (ppm)): 185.5, 178.4, 150.4, 147.0, 139.0, 134.7, 131.4, 130.7, 126.2, 126.0, 125.0, 121.3, 117.1, 116.9, 111.9, 111.6, 101.5, 28.4. *Anal.* calc. for C$_{31}$H$_{23}$IrN$_2$O$_4$ (MW = 679.75): C, 49.73; H, 2.83; N, 3.74. Found: C, 49.67; H, 2.90; N, 3.69%. MS (FAB; *m/z*): 680.2825.

4.16. Synthesis of bis[2-(4-chlorophenyl)benzoxazolato-N,C$^{2'}$]iridium(III) (acetylacetonate) (2)

Orange solid. 70% yield (based on the corresponding dimer). ^{1}H NMR (300 MHz, CDCl$_3$, 298 K; δ (ppm)): 7.73–7.38 (m, 10H), 7.41–7.22 (m, 1H), 6.93–7.90 (m, 2H), 6.41 (d, *J* = 1.8 Hz, 1H), 5.26 (s, 1H), 1.85 (s, 6H). ^{13}C NMR (75 MHz, CDCl$_3$, 298 K; δ (ppm)): 185.8, 150.3, 147.9, 138.6, 138.3, 137.5, 134.3, 129.4, 127.0, 126.9, 126.7, 126.4, 125.4, 122.3, 122.1, 117.2, 116.8, 111.9, 101.9, 101.6, 28.3, 27.9, 27.7. *Anal.* calc. for C$_{31}$H$_{21}$Cl$_2$IrN$_2$O$_4$ (MW = 748.64): C, 49.73; H, 2.83; N, 3.74. Found: C, 49.64; H, 2.89; N, 3.67. MS (FAB; *m/z*): 748.1827.

4.17. Synthesis of bis[2-phenyl-5-chlorobenzoxazolato-N,C$^{2'}$]iridium(III) (acetylacetonate) (3)

Orange solid. 50% yield (based on the corresponding dimer). ^{1}H NMR (300 MHz, CDCl$_3$, 298 K; δ (ppm)): 7.69–7.64 (m, 4H), 7.45–7.39 (m, 4H), 6.92–6.85 (m, 2H), 6.78–6.72 (m, 2H), 6.47 (d, *J* = 7.5 Hz, 2H), 5.24 (s, 1H), 1.82 (s, 6H). ^{13}C NMR (75 MHz, CDCl$_3$, 298 K; δ (ppm)): 185.7, 179.1, 150.6, 147.0, 137.8, 134.6, 131.8, 130.7, 130.1, 127.0, 126.3, 126.2, 121.7, 121.5, 117.2, 112.5, 112.4, 101.5, 28.4. *Anal.* calc. for C$_{31}$H$_{21}$Cl$_2$IrN$_2$O$_4$ (MW = 748.64): C, 49.73; H, 2.83; N, 3.74%. Found: C, 49.70; H, 2.85; N, 3.70%.. MS (FAB; *m/z*): 748.2119.

4.18. Synthesis of bis[2-(3,5-difluorophenyl)benzoxazolato-N,C$^{2'}$]iridium(III) (acetylacetonate) (4)

Orange solid. 80% yield (based on the corresponding dimer). ^{1}H NMR (300 MHz, CDCl$_3$, 298 K; δ (ppm)): 7.66 (d, *J* = 7.5 Hz, 2H), 7.51–7.32 (m, 8H), 6.29–6.22 (m, 2H), 5.31 (s, 1H), 1.87 (s, 6H). ^{13}C NMR (75 MHz, CDCl$_3$, 298 K; δ (ppm)): 185.7, 149.9, 139.6, 126.2, 125.6, 117.1, 111.7, 108.9, 108.8, 108.6, 108.5, 107.2, 106.9, 106.8, 106.4, 101.7, 28.2. *Anal.* calc. for C$_{31}$H$_{19}$F$_4$IrN$_2$O$_4$ (MW = 751.72): C, 49.53; H, 2.55; N, 3.73. Found: C, 49.51; H, 2.67; N, 3.74%. MS (FAB; *m/z*): 752.2380.

4.19. Synthesis of bis[2-(2-naphthyl)benzoxazolato-N,C$^{2'}$]iridium(III) (acetylacetonate) (5)

Red solid. 80% yield (based on the corresponding dimer). ^{1}H NMR (300 MHz, CDCl$_3$, 298 K; δ (ppm)): 8.21 (s, 2H), 7.79–7.77 (m, 2H), 7.68–7.63 (m, 4H), 7.55–7.45 (m, 6H), 7.23–7.12 (m, 6H), 6.82 (s, 1H), 1.85 (s, 6H). *Anal.* calc. for C$_{39}$H$_{27}$IrN$_2$O$_4$ (MW = 779.87): C, 60.06; H, 3.49; N, 3.59. Found: C, 60.02; H, 3.50; N, 3.55%. MS (FAB; *m/z*): 780.2987.

4.20. Synthesis of bis[2-(4-chlorophenyl)benzoxazolato-N,C$^{2'}$]iridium(III) (dibenzoylmethanate) (6)

Red solid. 82% yield (based on the corresponding dimer). ^{1}H NMR (400 MHz, CDCl$_3$, 298 K; δ (ppm)): 7.84–7.80 (m, 4H), 7.73–7.70 (m, 2H), 7.65–7.60 (m, 4H), 7.51–7.15 (m, 12H), 6.96–6.93 (m, 2H), 6.63 (s, 1H). ^{13}C NMR (75 MHz, CDCl$_3$, 298 K; δ (ppm)): 179.7, 177.2, 150.0, 149.7, 147.9, 140.2, 139.5, 138.2, 137.1, 134.2, 130.4, 129.3, 128.3, 126.9, 126.8, 126.5, 126.2, 125.6, 125.0, 124.7, 122.2, 121.9, 121.8, 117.1, 116.6, 115.0, 113.2, 111.5, 96.2, 95.3. *Anal.* calc. for C$_{41}$H$_{25}$Cl$_2$IrN$_2$O$_4$ (MW = 872.78): C, 56.42; H, 2.89; N, 3.21. Found: C, 56.12; H, 2.90; N, 3.16%. MS (FAB; *m/z*): 872.0827.

4.21. Synthesis of bis[2-(3,5-difluorophenyl)benzoxazolato-N,C$^{2'}$]iridium(III) (dibenzoylmethanate) (7)

Red solid. 85% yield (based on the corresponding dimer). ^{1}H NMR (300 MHz, CDCl$_3$, 298 K; δ (ppm)): 7.87–7.84 (m, 4H), 7.60 (d, *J* = 8.1 Hz, 2H), 7.45–7.32 (m, 12H), 7.20–7.15 (m, 2H), 6.71 (s, 1H), 6.36–6.29 (m, 2H). ^{13}C NMR (75 MHz, CDCl$_3$, 298 K; δ (ppm)): 179.9, 149.9, 140.1, 139.5, 130.8, 128.6, 127.2, 126.3, 125.5, 117.2, 111.7, 108.8, 108.4, 107.1, 106.8, 106.7, 106.4, 95.6. *Anal.* calc. for C$_{41}$H$_{23}$F$_4$IrN$_2$O$_4$ (MW = 875.85): C, 56.22; H, 2.65; N, 3.20. Found: C, 56.25 H, 2.66; N, 3.21%. MS (FAB; *m/z*): 876.3012.

4.22. Synthesis of bis[2-(2-naphthyl)benzoxazolato-N,C$^{2'}$]iridium(III) (dibenzoylmethanate) (8)

Red solid. 78% yield (based on the corresponding dimer). ^{1}H NMR (400 MHz, CDCl$_3$, 298 K; δ (ppm)): 8.23 (s, 2H), 7.86–7.83 (m, 4H), 7.72–7.69 (m, 4H), 7.56 (d, *J* 8.4 Hz, 2H), 7.43–7.35 (m, 4H), 7.29–7.15 (m, 12H), 6.92 (s, 2H), 6.68 (s, 1H). *Anal.* calc. for C$_{49}$H$_{31}$IrN$_2$O$_4$ (MW = 904.01): C, 65.1; H, 3.46; N, 3.10. Found: C, 65.56; H, 3.37; N, 3.16%. MS (FAB; *m/z*): 904.

4.23. Synthesis of bis[2-(3,5-difluorophenyl)benzoxazolato-N,C$^{2'}$]iridium(III) [1,1,1,5,5,5-hexafluoroacetylacetonate] (9)

Red solid. 90% Yield (based on the corresponding dimer). ^{1}H NMR (300 MHz, CDCl$_3$, 298 K; δ (ppm)): 7.71 (d, *J* = 8.1 Hz, 2H), 7.52–7.25 (m, 8H), 6.32–6.27 (m, 2H), 6.10 (s, 1H). ^{13}C NMR (75 MHz, CDCl$_3$, 298 K; δ (ppm)): 149.8, 138.8, 126.8, 126.2, 116.3, 112.1, 109.2, 109.1, 108.8, 107.7, 107.4, 107.3, 106.9, 92.9. *Anal.* calc. for C$_{31}$H$_{13}$F$_{10}$IrN$_2$O$_4$ (MW = 859.65): C, 43.31; H, 1.52; N, 3.26. Found: C, 43.40; H, 1.52; N, 3.24%. MS (FAB; *m/z*): 860.2679.

4.24. X-ray crystallography

The diffraction data of complexes **3**, **4**, and **7**–**9** were collected on a Bruker SMART APEX CCD diffractometer with graphite-mono-chromatized Mo Kα X-ray radiation ($\lambda = 0.71073$ Å) at room temperature. All the calculations for the structure determination were carried out using SHELXTL package (version 5.1) [25]. Initial atomic positions were located by Patterson methods using XS, and the structures of the complexes were refined by the least-square method using SHELXL-97. The structural analyses for complexes **4** and **7** proceeded smoothly, but disordered solvent molecules were observed from different maps for complex **3**, a slight packing disorder of one of the two nbo ligands was observed for complex **8**, and a packing disorder of F atoms of the ancillary ligand, hfpdo, was also observed for complex **9**. The final residuals of the final refinement were $R_1 = 0.0277$, $wR_2 = 0.0697$ for **3**, $R_1 = 0.0244$, $wR_2 = 0.0671$ for **4**, $R_1 = 0.0318$, $wR_2 = 0.0995$ for **7**, $R_1 = 0.0595$, $wR_2 = 0.1731$ for **8**, and $R_1 = 0.0212$, $wR_2 = 0.0482$ for **9**, respectively. Basic information pertaining to crystal parameters and structure refinement are summarized in Table 1. Selected bond distances and angles are listed in Table 2.

Acknowledgement

Appendix A. Supplementary material

CCDC 685736, 685737, 685738, 685739, 685740 contain the supplementary crystallographic data for this paper. These data can be obtained free of charge from The Cambridge Crystallographic Data Centre via www.ccdc.cam.ac.uk/data_request/cif. Supplementary data associated with this article can be found, in the online version, at doi:10.1016/j.jorganchem.2008.06.034.

References

[1] Z. Zhao, C.-Y. Jiang, M. Shi, F.-Y. Li, T. Yi, Y. Cao, C.-H. Huang, Organometallics 25 (2006) 3631.
[2] (a) Y.-T. Huang, T.-H. Chuang, Y.-L. Shu, Y.-C. Kuo, P.-L. Wu, C.-H. Yang, I.-W. Sun, Organometallics 24 (2005) 6230;
(b) X. Gong, S. Wang, D. Moses, G.C. Bazan, A.J. Heeger, Adv. Mater. 17 (2005) 2053;
(c) L. Chen, C. Yang, J. Qin, J. Gao, D. Ma, Inorg. Chim. Acta 359 (2006) 4207;
(d) R.R. Das, C.-L. Lee, Y.-Y. Noh, J.-J. Kim, Opt. Mater. 21 (2002) 143;
(e) L.-L. Wu, C.-H. Yang, I.-W. Sun, S.-Y. Chu, P.-C. Kao, Y. Cao, H.-H. Huang, Organometallics 26 (2007) 2017;
(f) F.-M. Hwang, H.-Y. Chen, P.-S. Chen, C.-S. Liu, Y. Chi, C.-F. Shu, F.-I. Wu, P.-T. Chou, S.-M. Peng, G.-H. Lee, Inorg. Chem. 44 (2005) 1344;
(g) C.-H. Yang, S.-W. Li, Y. Chi, Y.-M. Cheng, Y.-S. Yeh, P.-T. Chou, G.-H. Lee, C.-H. Wang, C.-F. Shu, Inorg. Chem. 44 (2005) 7770;
(h) H.-C. Li, P.-T. Chou, Y.-H. Hu, Y.-M. Cheng, R.-S. Liu, Organometallics 24 (2005) 1329.
[3] E. Mieczy'nska, M. Anna, A.M. Trzeciak, J. J'ozef, I. Kownacki, B.J. Marciniec, Mol. Catal. A 237 (2005) 246.
[4] (a) K. Ogata, A. Toyota, J. Organomet. Chem. 692 (2007) 4139;
(b) W.H. Bernskoetter, E. Lobkovsky, P.J. Chirik, Organometallics 24 (2005) 6250.
[5] P. Mura, A. Casini, G. Marcon, L. Messori, Inorg. Chim. Acta 312 (2001) 74.
[6] (a) I.J. Kim, Y.H. Kim, Y.S. Kim, Colloids Surf. A 313 (2008) 426;
(b) S. Lamansky, P. Djurovich, D. Murphy, A.-R. Feras, R. Kwong, I. Tsyba, M. Bortz, B. Mui, R. Bau, M.E. Thompson, Inorg. Chem. 40 (2001) 1704.
[7] L. Jian, P.I. Djurovich, B.D. Alleyne, M. Yousufuddin, N.N. Ho, J.C. Thomas, J.C. Peters, R. Bau, M.E. Thompson, Inorg. Chem. 44 (2005) 1713.
[8] A. Rzeska, J. Malicka, K. Guzow, M. Szabelski, W. Wicz, J. Photochem. Photobiol. A 146 (2001) 9.
[9] K. Guzowa, D. Szmigiel, D. Wr'oblewski, M. Milewska, J. Karolczak, W. Wiczk, J. Photochem. Photobiol. A 187 (2007) 87.
[10] E.-D.H. Safa, A.F. Tarek, N.Z. Saleh, J. Photochem. Photobiol. A 177 (2006) 238.
[11] A.F. Tarek, J. Photochem. Photobiol. A 121 (1999) 17.
[12] (a) A. Decken, A.G. Robert, J. Inorg. Biochem. 99 (2005) 664;
(b) X.-F. He, C.M. Vogels, A. Decken, S.A. Westcott, Polyhedron 23 (2004) 155;
(c) K. Tanaka, K.N. Sano, T. Kurushima, J. Fluor. Chem. 127 (2006) 1073.
[13] (a) K. Guzowa, M. Szabelskia, J. Karolczakb, W. Wiczka, J. Photochem. Photobiol. A 170 (2005) 215;
(b) S.-I. Um, Dyes Pigments 75 (2007) 185.
[14] K. Guzowa, D. Szmigiel, D. Wr'oblewski, M. Milewskaa, J. Karolczak, W. Wiczk, J. Photochem. Photobiol. A 187 (2007) 87.
[15] M. Guan, L. Gaob, S. Wang, C. Huanga, K. Wang, J. Lumin. 127 (2007) 489.
[16] (a) K.-Y. Ho, W.-Y. Yu, K.-K. Cheng, C.-M. Che, Chem. Commun. (1998) 2101;
(b) Z.K. Chan, T.-R. Chen, J.-D. Chen, J.-C. Wang, C.W. Liu, Dalton Trans. (2007) 3450;
(c) Z.K. Chan, T.-R. Chen, Y.-F. Tsai, J.-D. Chen, J.-C. Wang, Polyhedron 26 (2007) 3450.
[17] M.L. Glówka, D. Martynowski, K.J. Kozlowska, Mol. Struct. 474 (1999) 81.
[18] T. Sajoto, P.I. Djurovich, A. Tamayo, M. Yousufuddin, R. Bau, M.E. Thompson, Inorg. Chem. 44 (2005) 7992.
[19] K. Guzowa, M. Szabelskia, J. Karolczakb, W. Wiczka, J. Photochem. Photobiol. A 170 (2005) 215.
[20] T. Liu, B.-H. Xia, X. Zhou, H.-X. Zhang, Q.J. Pan, J.-S. Gao, Organometallics 26 (2007) 143.
[21] D.P. Rillema, C.B. Blanton, R.J. Shaver, D.C. Jackman, M. Boldaji, S. Bundy, L.A. Worl, T. Meyer, J. Inorg. Chem. 31 (1992) 1600.
[22] N.J. Turro, Modern Molecular Photochemistry, University Science Books, Mill Valley, CA, 1991.
[23] A.B. Tamayo, B.D. Alleyne, P.I. Djurovich, S. Lamansky, I. Tsyba, N.N. Ho, R. Bau, M.E. Thompson, J. Am. Chem. Soc. 125 (2003) 7377.
[24] Í. Ören, Ö. Temiz, Í. Yalçin, E. Sener, N. Altanlar, Eur. J. Pharm. Sci. 7 (1998) 153.
[25] G.M. Sheldrick, SHELXTL, version 5.1, Bruker Analytical X-ray System, Inc., Madison, WI, 1997.